Applied Thermal Engineering 161 (2019) 114190

Contents lists available at ScienceDirect

Applied Thermal Engineering

journal homepage: www.elsevier.com/locate/apthermeng

Research Paper

# Numerical modelling and transient analysis of a printed circuit heat exchanger used as recuperator for supercritical $CO_2$ heat to power conversion systems

Matteo Marchionni, Lei Chai, Giuseppe Bianchi*, Savvas A. Tassou

*Institute of Energy Futures, Centre for Sustainable Energy Use in Food Chains, Brunel University London, Uxbridge, Middlesex UB8 3PH, United Kingdom*

## HIGHLIGHTS

- A one-dimensional model for PCHEs is proposed and validated against 3-D CFD simulations.
- The one-dimensional methodology is used to model a 630 kW PCHE.
- Off-design performance maps of the heat exchanger are presented.
- Transient analyses are carried out to study the dynamic response of the device.

## GRAPHICAL ABSTRACT

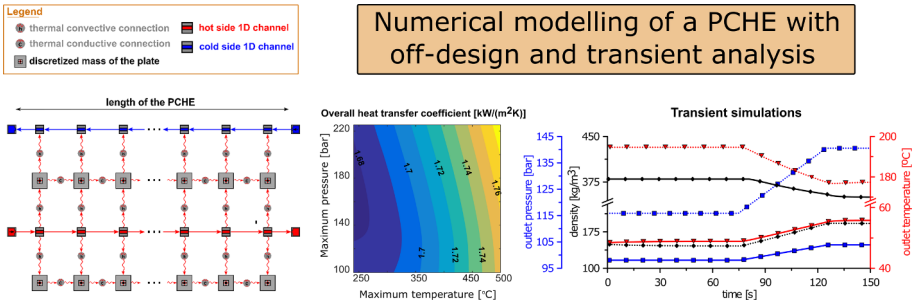


## ARTICLE INFO

*Keywords:*
Printed circuit heat exchanger
PCHE recuperator
CFD modelling
Transient simulations
$sCO_2$ power cycles

## ABSTRACT

The paper presents a modelling methodology for Printed Circuit Heat Exchangers (PCHEs) in supercritical $CO_2$ ($sCO_2$) power systems. The PCHE model can be embedded in models of the full $sCO_2$ power unit for optimisation, transient simulation and control purposes. In particular, the purpose of the study is to assess the potential and limitations of lower order models in predicting the overall heat transfer performance of PCHEs. The heat transfer processes in the channels of the PCHE recuperator are modelled in 1-D and 3-D using commercial software platforms. The results show that predictions from the two modelling approaches are in good agreement, confirming that the 1-D approach can be used with confidence for fast simulation and analysis of PCHEs. Using the 1-D approach, the model was validated against manufacturer's data for a 630 kW PCHE recuperator, and subsequently used to simulate the performance of the heat exchanger at design and off-design operating conditions. Performance maps produced from the simulations, enable visualization of the influence of operating conditions on the heat transfer performance and pressure drops in the heat exchanger. Dynamic simulations under transient operating conditions show that the thermal expansion of the working fluid caused by a fast reduction in density and increase in pressure in the system, can be a concern, requiring careful management of the start-up process to avoid sudden changes in temperature and thermal stresses.

## 1. Introduction

Heat to power conversion systems based on the Joule-Brayton cycle using supercritical carbon dioxide ($sCO_2$) as the working fluid are a promising technology for nuclear, concentrated solar power and high-temperature Waste Heat Recovery (WHR) applications [1,2]. Their

* Corresponding author.
*E-mail address:* giuseppe.bianchi@brunel.ac.uk (G. Bianchi).

https://doi.org/10.1016/j.applthermaleng.2019.114190
Received 16 February 2019; Received in revised form 1 July 2019; Accepted 27 July 2019
Available online 28 July 2019

**Nomenclature**

*Symbols*

| | |
|---|---|
| $\varepsilon$ | rate of dissipation of Turbulence energy [kW] |
| $C$ | calibration coefficient [–] |
| $D$ | diameter [m] |
| $f$ | fanning factor [–] |
| $k$ | turbulence kinetic energy [kJ] |
| $\bar{N}u_L$ | length averaged Nusselt number [–] |
| $Ra$ | surface roughness [μm] |
| $Re$ | REYNOLDS number [–] |

*Subscripts*

| | |
|---|---|
| $s$ | Surface |
| $D$ | diameter |

*Acronyms*

| | |
|---|---|
| 1-D | one-dimensional |
| 3-D | three-dimensional |
| CFD | Computational Fluid Dynamics |
| PCHE | Printed Circuit Heat Exchanger |
| $sCO_2$ | supercritical carbon dioxide |

main advantages over conventional power cycles are compactness and higher efficiency. The technology readiness level of $sCO_2$ power systems is, however, still low, and more research is needed to address some key technological challenges such as the development of reliable and cost-effective heat exchangers.

Heat transfer equipment for $sCO_2$ applications need to operate reliably at high temperatures and pressures. For economic viability of $sCO_2$ power systems, the cost of heat exchangers also needs to be reduced significantly from their current level which represents 80% of the cost of the whole system [3]. Amongst the possible configurations of the Joule-Brayton cycle, the recompression cycle [6–9] is the most attractive one given the enhanced performance that can be achieved from the use of two recuperators [10,11]. However, for small power outputs of the order of 100 kWe, the simple regenerative cycle becomes a good techno-economic trade-off [2]. In this Joule-Brayton cycle layout, at least three heat exchangers are needed: the gas cooler, the recuperator and the gas heater [4]. The recuperator performance has a significant impact on the cycle efficiency [5].

Printed Circuit Heat Exchangers (PCHEs) with zig-zag or wavy channels are the most established recuperator technology for $sCO_2$ power systems. Not only they can withstand severe thermal stresses and operating pressures up to 1000 bar, but can also provide high heat transfer rates while maintaining high compactness (80–200 kg/MW) [12]. A number of publications in the literature focus on experimental testing and three-dimensional (3-D) Computational Fluid Dynamics (CFD) modelling of these devices. The aim of these studies was mainly the investigation of the detailed fluid dynamic phenomena and the thermo-hydraulic performance of the heat exchangers.

Nikitin et al. [13] investigated the heat transfer and pressure drop characteristics of a PCHE with zig-zag channels using an experimental facility in the Tokyo Institute of Technology. The compactness of the test heat exchanger core was about 1,050 $m^{-1}$ and the maximum power density approached 4.4 $MW/m^3$, leading to overall heat transfer coefficient of between 300 and 650 $W/(m^2K)$. Empirical correlations to predict the heat transfer coefficient and pressure drops were proposed for the tested PCHE, but these correlations just referred to the Reynolds number. With the same experimental facility, Ngo et al. in [14] tested another PCHE and proposed correlations for the Nusselt number and friction factor.

Lee and Kim [15–19] used the shear stress transport (SST) turbulence model to study the effects of the geometric parameters of zig-zag flow channels on the thermo-hydraulic performance in the Reynolds number range 65,000–270,000. The geometric parameters tested were the channel angle, the ellipse aspect ratio of the channel, the pitch ratio, the rib depth and the hydraulic diameter of the channel, together with four different shapes of channel cross section. The results showed that the rectangular channel had the best thermal performance but also the worst hydraulic performance. Kim et al. [20] developed a k-epsilon ($k$-$\varepsilon$) SST turbulence model considering $CO_2$ real gas properties. Based on comparison between simulation and experimental results, they proposed Nusselt number and friction factor correlations covering an extended range of Reynolds numbers, between 2000 and 58,000.

Baik et al. [21] investigated the effects of additional geometric parameters such as the waviness factors (including the amplitude and the period of waviness) on the thermal performance of PCHE. The wavy-channel PCHE showed a significantly higher thermal performance than the straight-channel, mainly due to the increased heat transfer area. To improve the performance of the zig-zag channel PCHE, Lee et al. [22] proposed a zig-zag channel PCHE with straight junctions at the bends, and carried out 3-D numerical analysis using the re-normalization group (RNG) $k$-$\varepsilon$ turbulence model. Through a comparison of the dimensionless factors, including the Fanning friction factor, Colburn-j factor, and volume-goodness factor, this particular channel shape was found to have a better thermo-hydraulic performance than the more conventional zig-zag one.

Despite the extensive research on the thermo-hydraulic performance of PCHEs, the complex models presented in the literature are not suitable for overall system modelling, optimisation and control. This limitation is mostly due to the high computational effort required for 3-D CFD calculations in which the thermo-physical properties of the working fluid must be coupled with the solution of the conservation equations. The steep variation of $CO_2$ properties in the critical region indeed requires a deep resolution of these trends in order to achieve accurate results. Property linearization within the simulation range like the one performed in the thermal circuit method of simulation [23–25] cannot be applied in the context of supercritical $CO_2$ due to the large variation in property values close to the critical point.

In the current research work, we propose and analyse a simulation methodology for PCHEs based on the one-dimensional (1-D) modelling approach. To the authors' knowledge, this method, although it has been extensively employed in the automotive simulation field, it has not been applied to $sCO_2$ power systems before. As such, in order to assess its scientific soundness, i.e. potential and limitations, a benchmark against results from higher order models (3-D RANS CFD) is also presented. In particular, the comparison between 1-D and 3-D CFD results is carried out with reference to an elementary heat transfer unit of a PCHE recuperator. After this assessment, the 1-D methodology has been applied to a 630 kW recuperator of a $sCO_2$ experimental facility at Brunel University London. The $sCO_2$ system which has a nominal power output of 50 kWe is based on the simple regenerated $sCO_2$ cycle layout [26]. After calibration of the model against manufacturer's data, off-design performance maps of the PCHE have been developed and presented together with transient analysis for start-up, shutdown and change of operating conditions in the $sCO_2$ power system.

## 2. Modelling methodologies

The structure of a PCHE is characterized by a high number of equally spaced channels with identical geometrical features. As such, a heat exchanger can be modelled as a series of elementary heat transfer units composed of a pair of channels surrounded by solid substrates and periodic boundary conditions. The geometric features and materials of

**Table 1**
Geometrical features and materials of the elementary heat transfer unit.

| | |
|---|---|
| Wetted perimeter [mm] | 5.14 |
| Hydraulic diameter [mm] | 1.22 |
| Cross-sectional area [mm$^2$] | 1.57 |
| Length [mm] | 272.00 |
| Plate thickness [mm] | 1.63 |
| Surface roughness | Neglected |
| Material | Stainless steel 316L |

**Table 2**
Boundary conditions used for the models comparison.

| Boundary conditions | Cold side | Hot side |
|---|---|---|
| Mass flux [kg/m$^2$] | 509.3 | |
| Inlet temperature [°C] | 100 | 400 |
| Outlet pressure [bar] | 150 | 75 |

the PCHE used in this investigation are summarised in Table 1, while Table 2 lists the boundary conditions considered in the simulations.

### 2.1. 3-D approach

The symmetry axis of the elementary PCHE unit is located in the middle of the semi-circular channel cross-section. With reference to Fig. 1, the computational domain is composed of half hot channel (depicted in red), half cold channel (depicted in blue), and surrounding stainless steel substrate (depicted in grey). The periodic boundary conditions, which refer to the heat transfer rates between the channels, are set on the top and bottom surfaces of the elementary heat transfer unit [27].

The data in Tables 1 and 2 were used to assess the nature of the flow. The Reynolds number was found to be higher than 10,000 in both the cold and hot sides of the heat exchanger, confirming turbulent flow, which was modelled using the standard k-ε approach with standard wall factions. The buoyancy and entrance effects were also considered. The thickness of the first near-wall mesh was selected to ensure the dimensionless distance from the wall $y^+$ in the range between 15 and 50. To account for the variation of the thermophysical properties of the $CO_2$ due to variations in temperature and pressure, the NIST Refprop database was coupled with the ANSYS™ FLUENT 17.0 CFD solver through a Dynamic-Link Library (DLL) [28]. The SIMPLEC algorithm was used to implement the coupling between pressure and velocity, while the second order upwind scheme was applied to discretize the convection terms. A grid independence study was carried out using different mesh sizes listed in Table 3. The computational grid selected for the model, shown in Fig. 2, comprised of 1.8 million cells.

### 2.2. 1-D approach

The 1-D model of the elementary heat transfer unit was developed in the commercial tool GT-SUITE™. The semi-circular flow channels of the PCHE shown in Fig. 1, were considered as circular channels of an equivalent hydraulic diameter. In particular, the hot and cold channels (red and blue colours respectively) were discretized along the flow direction in a fixed number of sub-volumes (80 per channel), as shown in Fig. 3.

Each flow channel block is connected through a convective connection (grey circle denoted by the letter “h” in Fig. 3) to a discretized metallic mass, which represents the metal portion of the elementary PCHE unit delimited by the two sub-volumes of the channels (the grey square with a red point in the centre, Fig. 3). This metallic mass represents the discretized thermal inertia of the heat exchanger, which is calculated from the geometrical features and the material properties of the metallic substrate (i.e. the thermal conductivity and the density) specified as inputs. The discretized thermal masses, shown in Fig. 3 with grey boxes, are all interrelated by means of conductive connections to take into account the conductive heat transfer between them.

To solve the momentum and energy equations, the computation of the Fanning factor $C_f$ and the heat transfer coefficient $h$is needed. The first was calculated using the explicit approximation of the Colebrook equation proposed by Serghides [29] and reported in Eq. (1), which is

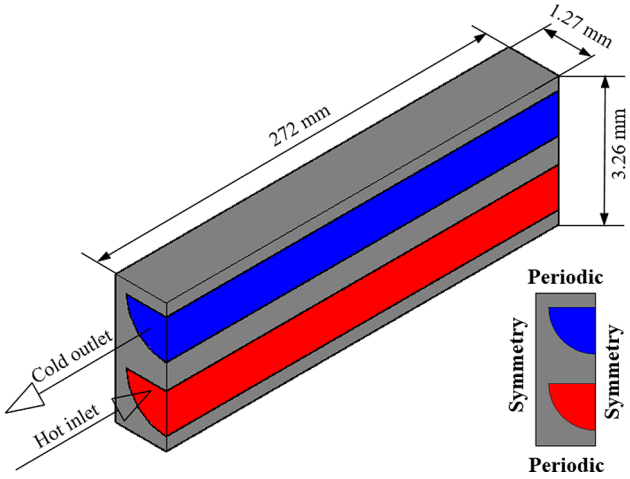


**Fig. 1.** Elementary heat transfer unit of a PCHE.

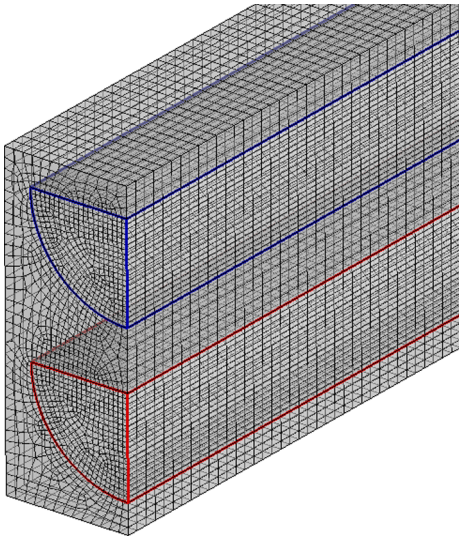

**Fig. 2.** Computational grid (1.8 million cells).

**Table 3**
Grid sensitivity study of the 3-D model.

| Number of cells | Cold side pressure drop [kPa] | Hot side pressure drop [kPa] | Cold side heat transfer coefficient [W/(m$^2$·K)] | Hot side heat transfer coefficient [W/(m$^2$·K)] |
|---|---|---|---|---|
| 352,658 | 3.946 | 8.177 | 2065.3 | 2091.1 |
| 704,898 | 3.837 | 8.276 | 2032.1 | 2078.1 |
| 1,843,953 | 3.763 | 8.342 | 1997.6 | 2052.6 |
| 3,686,753 | 3.749 | 8.355 | 1982.8 | 2037.5 |

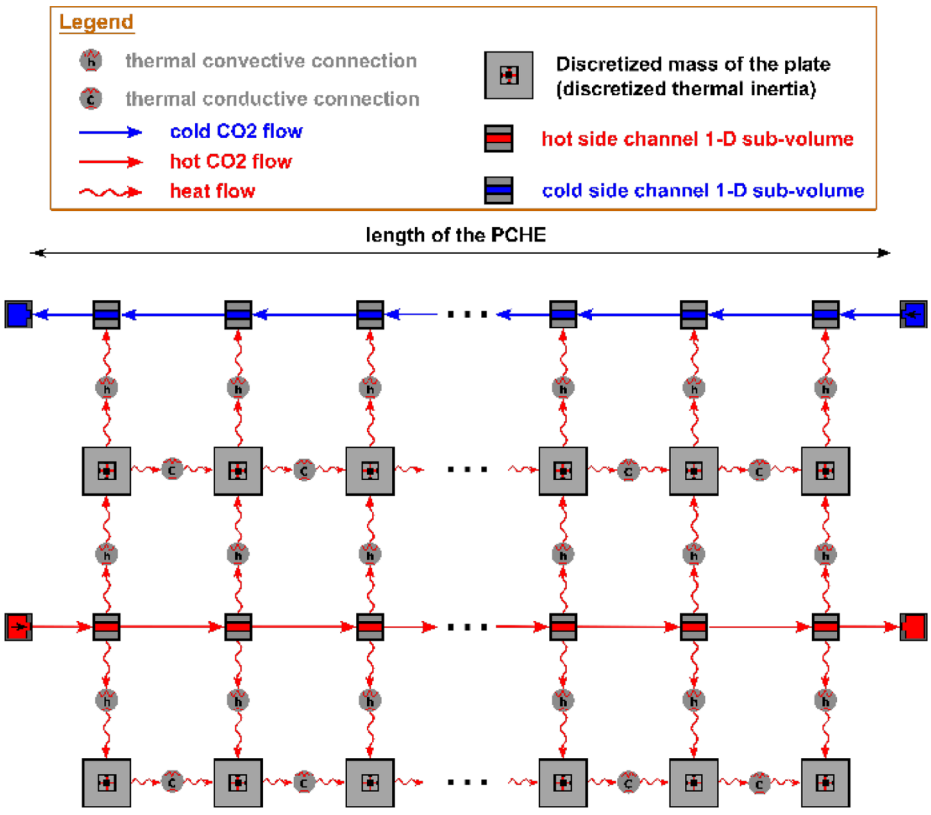


**Fig. 3.** 1-D model of the PCHE elementary heat transfer unit.

valid for the turbulent regime ($Re_D > 2100$). The quantities $A$ and $B$in Eq. (1) are reported in Eqs. (2) and (3) respectively and account for the roughness of the ducts $Ra$.

$$f = C_1\left(\frac{1}{4}\left(4.781 - \frac{(A-4.781)^2}{B-2A+4.781}\right)^{-2}\right) \quad (1)$$

$$A = -2.0\log_{10}\left(\frac{Ra/_D}{3.7} + \frac{12}{Re_D}\right) \quad (2)$$

$$B = -2.0\log_{10}\left(\frac{Ra/_D}{3.7} + \frac{2.51A}{Re_D}\right) \quad (3)$$

The heat transfer coefficient is predicted using the Gnieliski correlation [30] reported in Eq. (4).

$$N\bar{u}_L = C_2\left(\frac{(f/2)(Re-1000)Pr}{1+12.7(Pr^{2/3}-1)\sqrt{f/2}}\right) \quad (4)$$

Further inputs to the model are: the mass flow rate of the working fluid (which is equal for both the cold and the hot side of the heat exchanger), and the inlet temperatures and pressures of the hot and the cold $sCO_2$ flows (Table 2). A thorough description of the modelling procedure can be found in reference [31]. Also for the 1-D case, a grid independence study has been carried out and it is summarized in Table 4. The discretisation length used for the simulations is 3.4 mm.

### 2.2.1. Calibration procedure

The friction factor and Nusselt number correlations reported in Eqs. (1) and (4) were originally developed for circular heat transfer channels with known surface roughness. Should these assumptions fall, as in the current study, the formulations in question can still be used provided that a calibration against either experimental data or higher order models is performed. The purpose of the calibration is to retrieve the values of the calibration coefficients for friction factor and Nusselt number. These coefficients are $C_1$ in Eq. (1) and $C_2$in Eq. (4) respectively. The calibration procedure is performed through a least squares method between 1-D simulations and reference data for at least 5–10 operating points.

In the comparison between 1-D and 3-D CFD models reported in Section 3, the calibration of friction factor and Nusselt number correlations has not been carried out since both the modelling approaches neglected the channel surface roughness and because the purpose of the study was to highlight any correspondence or misalignment between the simulation results.

On the other hand, the analysis on the 630 kW PCHE presented in Section 4, required a calibration of the 1-D model given: the availability of the reference data provided by the manufacturer; the lack of information on the channel surface roughness; the zig-zag layout of the

**Table 4**
Grid sensitivity study for the 1-D model.

| Discretization length [mm] | Cold side pressure drop [kPa] | Hot side pressure drop [kPa] | Cold side heat transfer coefficient [W/(m²·K)] | Hot side heat transfer coefficient [W/(m²·K)] |
|---|---|---|---|---|
| 13.6 | 4.024 | 8.931 | 2238.7 | 2174.6 |
| 6.8 | 4.093 | 8.799 | 2254.9 | 2163.0 |
| 3.4 | 4.110 | 8.761 | 2257.4 | 2161.5 |
| 1.7 | 4.114 | 8.746 | 2258.6 | 2161.0 |

channels that a one-dimensional modelling methodology is incapable to take into account.

## 3. Comparison of CFD model results

Both 1-D and 3-D simulations were performed with reference to the boundary conditions reported in Table 2. Based on the grid independent studies, the spatial discretisation of the channel length was 0.05 mm in the 3-D model and 3.40 mm in the 1-D model. From a computational perspective, the 3-D simulation was run on an Intel Xeon E5-2670 CPU at 2.6 GHz which required 2.9 GB of RAM; the 1-D simulation was performed on an Intel Core i7-6700 CPU at 3.4 GHz which required 0.4 GB of RAM. The full CFD 3-D simulation case required 24 h to run, whilst a test run for the 1-D simulation only required 5 s. This fact confirms why 1-D modelling approaches are suitable for transient simulations and complex optimization studies. The higher computational time needed by the 3-D approach is not only due to the larger computational domain but also to the DLL interface with the Refprop database. Due to the high computational time and cost of the 3-D simulations, this benchmarking study considered a channel length for the PCHE of only 272 mm. This choice led to a very large approach temperature in the results, which is an operating condition not representative of an actual regenerative process. However, this did not influence the results comparison of the two modelling approaches.

Fig. 4 shows the comparison of the temperature profiles for the two $sCO_2$ flows in the PCHE as a function of the channel length. The temperatures along the channel obtained by the 1-D simulation match well that from the 3-D simulations, with a maximum relative error of 5% for the hot side and 8% for the cold side of the heat exchanger. The cumulative pressure drops along the channel length computed by the two models are shown in Fig. 5. In this case, the highest difference is shown at the entrance of the channel, where the pressure drops predicted by the 1-D model are 8.9 kPa and 4.0 kPa for the hot and cold sides respectively. For the 3-D model, hot and cold side pressure drops are 8.3 kPa and 3.8 kPa respectively. The differences are mainly due to the fact that the empirical correlations used in the 1-D simulation for the friction factor were based on circular tubes (since the modelling approach approximates the semi-circular channel cross-section with an equivalent circular one), while the 3-D simulations consider semi-circular channels. These conclusions agree with the findings in [32]; this study indeed shows that, for the same hydraulic diameter, friction factor in semi-circular channels is about 4.5% smaller than the one in circular tubes.

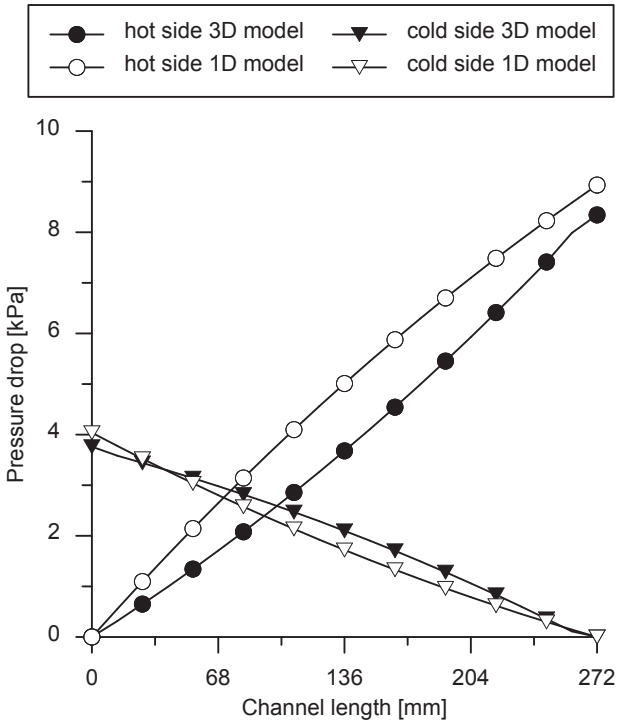


**Fig. 5.** Comparison of pressure drops along the PCHE channel from 1-D and 3-D simulations.

The estimation of the local heat transfer coefficients with the two models is presented in Fig. 6. With reference to the middle cross-section

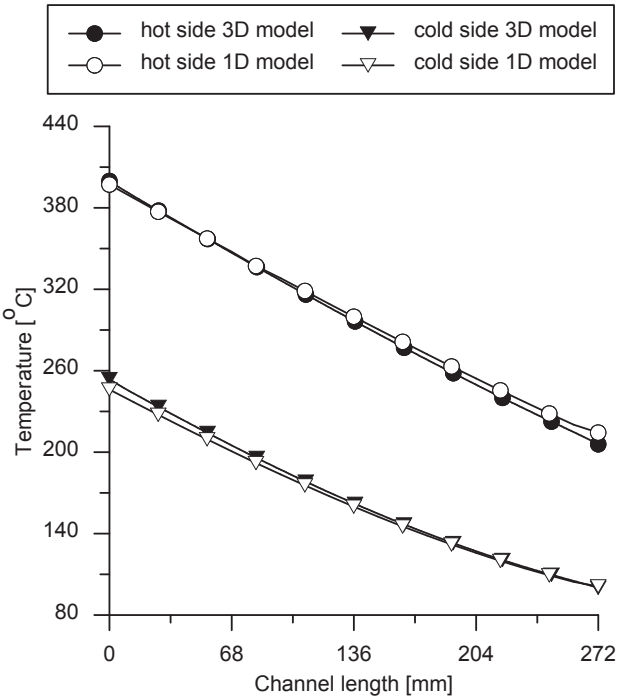


**Fig. 4.** Temperatures comparison along the PCHE channel resulting from 1-D and 3-D simulations.

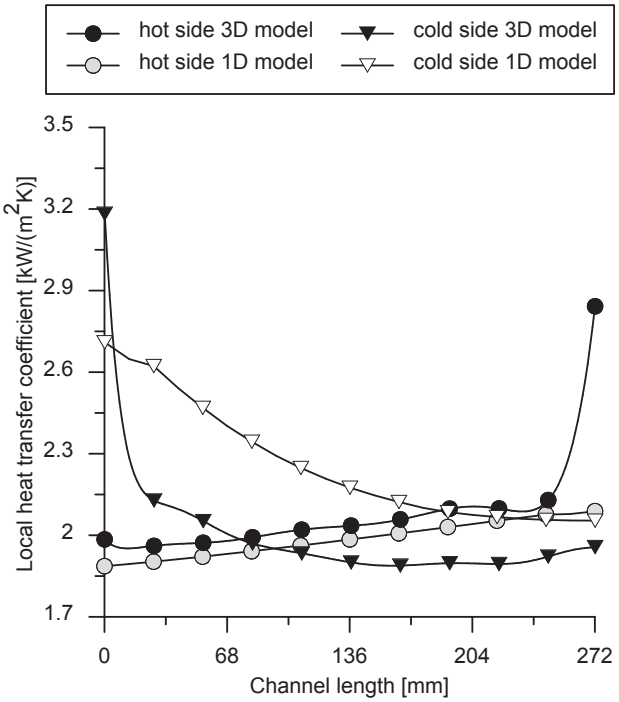


**Fig. 6.** Comparison of local convective heat transfer coefficient along the PCHE channel from 1-D and 3-D simulations.

(136 mm from the channel entry cross-section), the local heat transfer coefficient of the cold side was determined to be 1.90 kW/(m$^2$ K) with the 3-D model and 2.16 kW/(m$^2$ K) with the 1-D model. For the hot side, the value of the local heat transfer coefficient was predicted at 2.04 kW/(m$^2$ K) with the 3-D model and 1.98 kW/(m$^2$ K) with the 1-D model. The difference in the predictions of the local heat transfer coefficients with the two models is due to the correlation for circular tubes for the channels used in the 1-D case, which can contribute to an error in the calculation of the Nusselt number of up to 9% [32], and the different calculation procedure for the local heat transfer coefficient by the two models. In fact, the 3-D model computes the heat transfer coefficient from the geometrical properties of the channel and the velocity and thermal field for each cross section. The 1-D model does not account for the effect of the temperature difference between the channel wall and the one of the bulk fluid and large differences between the two temperatures can give rise to increased errors in the prediction [33]. The 1-D model, unlike the 3-D one, also does not account for the entry effects to the heat exchanger and this, as can be seen in Fig. 6, can lead to further differences in the predictions.

Despite the different local heat transfer coefficients calculated by the two models, the predictions of the global performance of the heat exchanger is very close. For the same inputs, the computed outlet temperature of the hot side of the heat exchanger is 213.4 °C and 205.8 °C for the 1-D and 3-D models respectively and for the hot side 246.2 °C and 253.9 °C respectively, a difference of only 4% and 3%. The percentage deviation of the overall heat transfer coefficient was found to be 2%, and a value of 7% and 5% were found for the pressure drops across the hot and cold sides respectively. These prediction differences are quite small, and much smaller than experimental uncertainties [34], and thus it can be concluded that the 1-D model can be used with confidence for fast simulation of the overall performance of the heat exchanger.

**Table 5**
PCHE channel geometry.

| | |
|---|---|
| Wetted perimeter [mm] | 5.14 |
| Hydraulic diameter [mm] | 1.22 |
| Cross-sectional area [mm$^2$] | 1.57 |
| Length [mm] | 1012.00 |
| Type | Zig-zag |

**Table 6**
Additional PCHE features.

| Material | SS 316L |
|---|---|
| Channel surface roughness | Not available |
| Channel discretization length [mm] | 25.30 |
| Number of channels per row | 54 |
| Number of rows | 42 |

## 4. Results and discussion

After the benchmarking of the 1-D modelling methodology against the 3-D CFD results, the one-dimensional approach has been employed to model the 630 kW PCHE recuperator that will be used in the $sCO_2$ heat to power cycle test rig currently being developed at Brunel University London [26,35]. Because the unit is designed to address WHR applications, the system configuration and pressure and temperature operating range were selected to minimise capital cost and maximise return on investment. This is reflected in the low inlet pressures and temperatures on the hot and cold sides of the PCHE. Design and off-design data provided by the manufacturer were used to calibrate the heat exchanger model, which was subsequently used to generate performance maps for different operating conditions. The dynamic behaviour of the heat exchanger was also modelled to investigate its transient behaviour during start-up, shut-down and rapid change in operating conditions.

### 4.1. Full scale PCHE model development and calibration

The 630 kW PCHE comprises 42 stainless steel 316L metal plates chemically etched to 54 semi-circular channels per plate which are bonded together through thermal diffusion. Tables 5 and 6 summarise the specification of the channels and heat exchanger respectively.

The calibration data provided by the manufacturer relate to five different working points of the PCHE which are not referred to particular operating conditions of the heat exchanger or the $sCO_2$ system (Table 7). Nonetheless, they have been chosen to appreciate the variability of the heat transfer performance. This approach justifies the selection of mass flow rate and temperature as exploratory variables rather than pressures. In fact, mass flow rate has a direct impact on the Reynolds number while temperature variations reflect their greater influence on changes in the thermophysical properties of the working fluid compared to pressure variations.

In the calibration procedure, a regression analysis was used to minimize the error between the data provided by the manufacturer and the predictions given by the chosen heat transfer and pressure drop correlations as highlighted in paragraph 2.2.1. Heat transfer and friction multiplier coefficients, which can be set for each of the working fluid phases, have been adjusted to minimize this error and to account for the additional pressure drops and the higher heat transfer rates for the zig-zag shape of the channels, whose effects cannot be reproduced by considering just a one-dimensional approach. Values for $C_1$ in Eq. (1) and $C_2$ in Eq. (4) after calibration were greater than one, namely 1.1 and 1.2 respectively. These magnitudes are in agreement with the theory since rough walls lead to greater pressure drops than smooth ones. Moreover, rough and the zig-zag channels have better heat transfer performance than smooth and straight ones.

Table 7, which refers to the calibration procedure of the PCHE, shows that the predictions of the model are in agreement with the

**Table 7**
Off-design operating conditions of the full scale PCHE (cold side (cs) and hot side (hs)).

| | Design | | Off-design #1 | | Off-design #2 | | Off-design #3 | | Off-design #4 | |
|---|---|---|---|---|---|---|---|---|---|---|
| | 1-D | OEM | 1-D | OEM | 1-D | OEM | 1-D | OEM | 1-D | OEM |
| mass flow rate [kg/s] | 2.06 | | 1.57 | | 2.09 | | 2.09 | | 2.62 | |
| cs inlet temperature [°C] | 72.9 | | 72.9 | | 87.5 | | 62.0 | | 72.9 | |
| cs inlet pressure [bar] | 125 | | 125 | | 125 | | 125 | | 125 | |
| hs inlet pressure [bar] | 75 | | 75 | | 75 | | 75 | | 75 | |
| hs inlet temperature [°C] | 344.3 | | 344.3 | | 344.3 | | 344.3 | | 344.3 | |
| hs pressure drop [kPa] | 131 | 130 | 80 | 79 | 146 | 145 | 123 | 122 | 205 | 202 |
| hs outlet temperature [°C] | 81.4 | 80.5 | 79.5 | 78.6 | 99.4 | 99.7 | 67.7 | 66.6 | 83.6 | 82.7 |
| cs pressure drop [kPa] | 119 | 120 | 73 | 74 | 138 | 139 | 104 | 106 | 183 | 184 |
| cs outlet temperature [°C] | 283.0 | 284.9 | 285.4 | 287.2 | 293.2 | 294.5 | 267.7 | 269.3 | 280.1 | 282.3 |
| heat load [kW] | 629 | 631 | 484 | 485 | 588 | 586 | 682 | 684 | 789 | 793 |

manufacturer's data. The results of the pressure drop calculations show the highest error to be 5.7% on the cold $CO_2$ flow for the 4th off-design case (working fluid mass flow rate of 2.62 kg/s, at 125% of the design value). Average errors are 1.1% and 2.2% for the hot and cold sides respectively. Also, the outlet temperatures and the heat loads computed, present negligible deviations compared to the manufacturer's data. The average errors for the cold and hot side outlet temperatures are 2.2% and 1.2% respectively, and the error for the overall heat transfer across the heat exchanger is only 1.2%.

### 4.2. Performance maps

The series of simulations presented in Fig. 7 were carried out to investigate the off-design behaviour of the PCHE. The purpose of this analysis was to show the impact on changes in the operating pressure and temperature on the performance of the recuperator. All the maps report 'maximum temperature' ($T_{max}$) and 'maximum pressure' ($p_{max}$) as independent variables. The maximum temperature in a $sCO_2$ recuperator occurs at inlet of the hot side of the heat exchanger while the maximum pressure is the one at the cold side inlet. In a real $sCO_2$ power system based on a simple regenerative Joule-Brayton cycle layout, these parameters depend on the turbomachine operation, namely compressor outlet pressure for the maximum inlet pressure of the recuperator and turbine outlet temperature for the maximum inlet temperature of the hot side. In terms of thermal power exchanged, important parameters are the overall heat transfer coefficient, the effectiveness and the total pressure drops in the PCHE, i.e. the sum of pressure drops on the hot and cold sides. Results are presented for simulations carried out at constant $CO_2$ mass flow rate, namely 1.57 kg/s (Fig. 7a–d), 2.09 kg/s (Fig. 7e–h) and 2.62 kg/s (Fig. 7i–n).

#### 4.2.1. Variation of mass flow rate

For given inlet pressures and temperatures of the hot and cold streams, a change in the operating $CO_2$ mass flow rate implies a direct effect on the Reynolds and, in turn, Nusselt numbers due to a variation in the flow velocity on both sides of the recuperator. This change, affects the thermo-hydraulic performance of the heat exchanger. With reference to a maximum temperature at the hot side inlet of 350 °C and a maximum inlet pressure at the cold side of the recuperator of 125 bar, in the three reference mass flow rates of 1.57 kg/s, 2.09 kg/s and 2.62 kg/s, the thermal power exchanged (Fig. 7a, e and i) is equal to 505 kW, 680 kW and 810 kW respectively. The increase in heat transfer rate is due to the greater overall heat transfer coefficient that, according to Fig. 7b, f and j, assumes values of 1.55 kW/($m^2$ K), 1.70 kW/($m^2$ K), 1.85 kW/($m^2$ K). As mentioned at the beginning of this paragraph, this trend depends on the high flow velocity.

On the other hand, as the mass flow rate increases, the total pressure drops in the heat exchanger also increase. In particular, as it can be noticed from Fig. 7d, h and n at $T_{max}$ 350 °C and $p_{max}$ 125 bar, the total pressure drops at 1.57 kg/s, 2.09 kg/s and 2.62 kg/s increase from 1.6 bar to 2.6 bar and 4.0 bar respectively.

Hence, a variation in the operating mass flow rate has two fold effects on the heat exchanger performance. On the contrary, negligible effects can be noticed on the heat exchanger effectiveness, since the mass flow rate term appears both at the numerator and denominator of the effectiveness expression. The slight differences noticed in Fig. 7c, g and m depend on the temperature variations that the different mass flow rates imply at the outlet of the heat exchanger. In particular, at $T_{max}$ 350 °C and $p_{max}$ 125 bar, the effectiveness at 1.57 kg/s, 2.09 kg/s and 2.62 kg/s decreases from 81% to 80% and 79% respectively.

#### 4.2.2. Maximum pressure variation

For a given mass flow rate and inlet temperatures of the hot and cold streams, if the maximum pressure at the cold side inlet of the heat exchanger varies but the temperature on the hot side inlet remains constant, the pressure ratio across the metallic parts of the device will be clearly affected. The pressure variation affects the density of the $CO_2$ and, consequently, the flow velocity on the cold side of the heat exchanger since the simulations reported in Fig. 7 are carried out at constant mass flow rate. In particular, the percentage variations of density and flow velocity are the inverse.

With reference to a maximum temperature at the hot side inlet of 350 °C and mass flow rate of 2.09 kg/s (Fig. 7e–h), if the pressure at the inlet of the hot side of the recuperator is kept at 75 bar while the one on the cold side rises from 120 bar, to 160 bar and 200 bar, the thermal power exchanged (Fig. 7e) reduces from 690 kW to 620 kW and 580 kW respectively. The decreasing trend in heat transfer rate depends on the lower flow velocity. The decrease of heat exchanger effectiveness at high pressure relates to the lower thermal power exchanged. The non-linear relationship between flow velocity and pressure drops eventually leads to a decrease in total pressure drop shown in Fig. 7h.

#### 4.2.3. Maximum temperature variation

A variation of the inlet temperature on the hot side of the heat exchanger is different to the case presented in paragraph 4.2.2. Indeed, even though the temperature also affects the fluid density, in this case the relationship is not direct as in the case of the pressure: if the temperature increases, in the current case also the flow velocity increases to compensate the reduction in fluid density caused by the pressure. Based on the analysis carried out in the previous paragraphs, an increase in the maximum temperature of the heat exchanger will imply higher heat transfer rates (Fig. 7a, e, i) but also larger pressure drops (Fig. 7d, h, n). Unlike the effects of increasing mass flow rate and pressure, an increase in temperature has positive benefits on the effectiveness of the recuperator.

The results from the above analysis should be taken into consideration in the selection of the recuperator for $sCO_2$ power systems. Amongst the main challenges in enhancing the efficiency of $sCO_2$ systems, are the high thermal duties heat exchangers have to operate at, and pressure drops along the cycle. High pressure drops in the components, limit the maximum expansion ratio across the turbine, which in turn influences the net power output. Similarly, the off-design study shows that for the recuperator, interrelationships between maximum cycle pressure and temperatures and $CO_2$ mass flow rate have to be addressed during the selection of the cycle operating parameters. Even though a high maximum cycle temperature is always beneficial in terms of turbine efficiency and net power output, it also increases the pressure drop in the PCHE therefore reducing the available expansion ratio across the turbine. Similarly, increasing the maximum cycle pressure leads to a higher cycle pressure ratio and to a reduction of the pressure drops (Fig. 7d, h and n) in the recuperator. At the same time this decreases the recuperator effectiveness and thus requires a larger device to accommodate the same thermal duty, i.e. higher capital expenditures due to the need to oversizing the heat exchanger to cope with these operating conditions.

### 4.3. Transient operating conditions

The transient behaviour of the PCHE was investigated with reference to three typical operating conditions for $sCO_2$ power systems, namely start-up (Fig. 8), shutdown (Fig. 9) and change of operating conditions (Fig. 10). The transient profiles for mass flow rate and inlet pressures and temperatures on both sides of the recuperator have been taken from the literature and refer to the experimental activity reported in [36]. In each figure, chart (a) shows the transient inputs to the simulation while chart (b) reports density, temperature and pressure at the outlet of the heat exchanger. Solid lines are used for the quantities related to the hot side of the recuperator and dashed lines for the cold side.

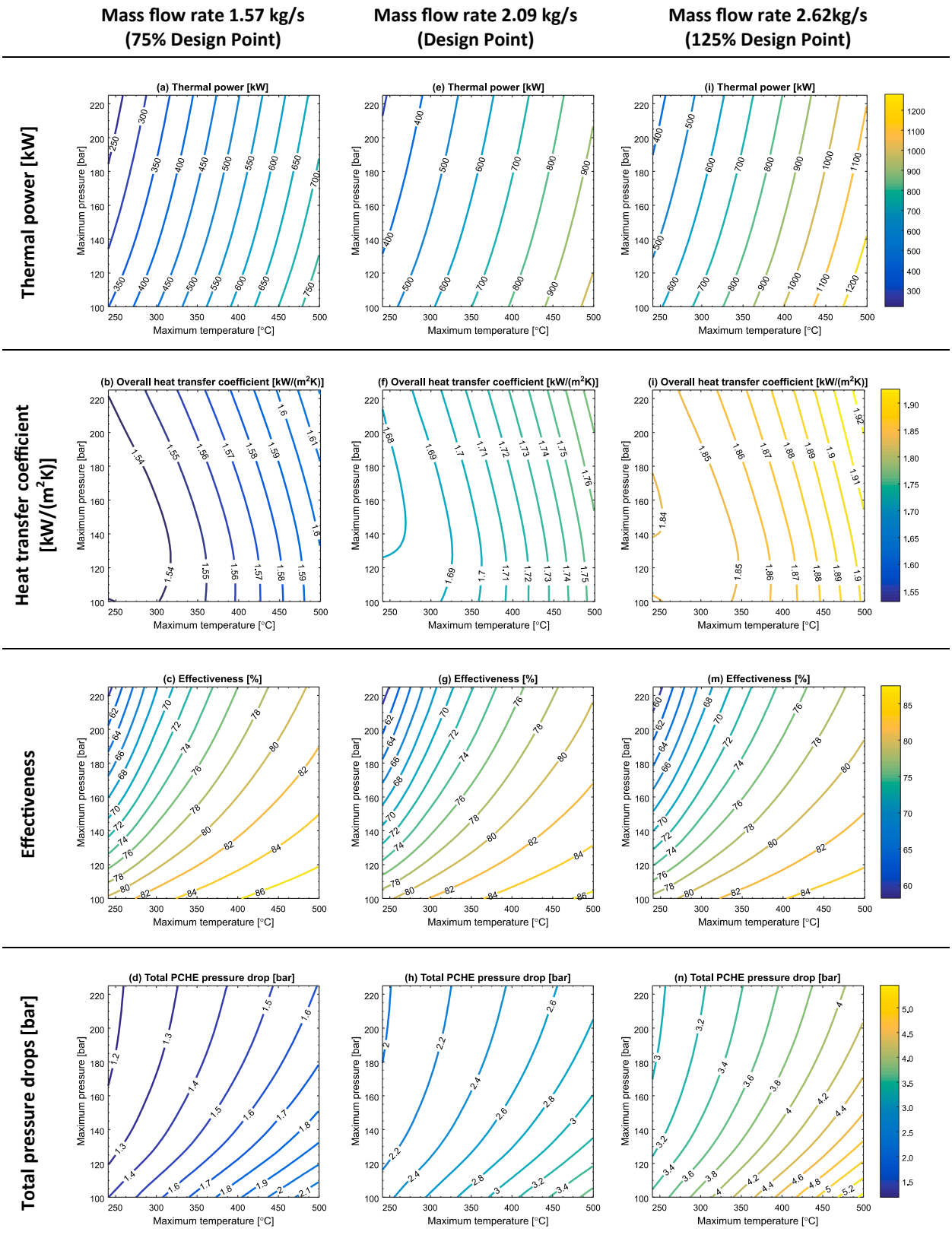


**Fig. 7.** Off-design performance maps of the PCHE for different values of $sCO_2$ mass flow rates: 1.57 kg/s (a–d), 2.09 kg/s (e–h) and 2.62 kg/s (i–n).

#### 4.3.1. Start-up

Fig. 8.a shows the initial conditions of the streams during the start-up of the $sCO_2$ power unit. The $CO_2$ mass flow rate increases from 0.10 kg/s to the steady state value of 2.06 kg/s in approximately 5 s. This steep increase is due to the increase in the compressor speed, which also leads to a rapid increase of the pressure on the cold side of the PCHE which rises to 96 bar. In approximately 20 s, the inlet temperature of the hot and cold sides reach 278 °C and 55 °C respectively. It

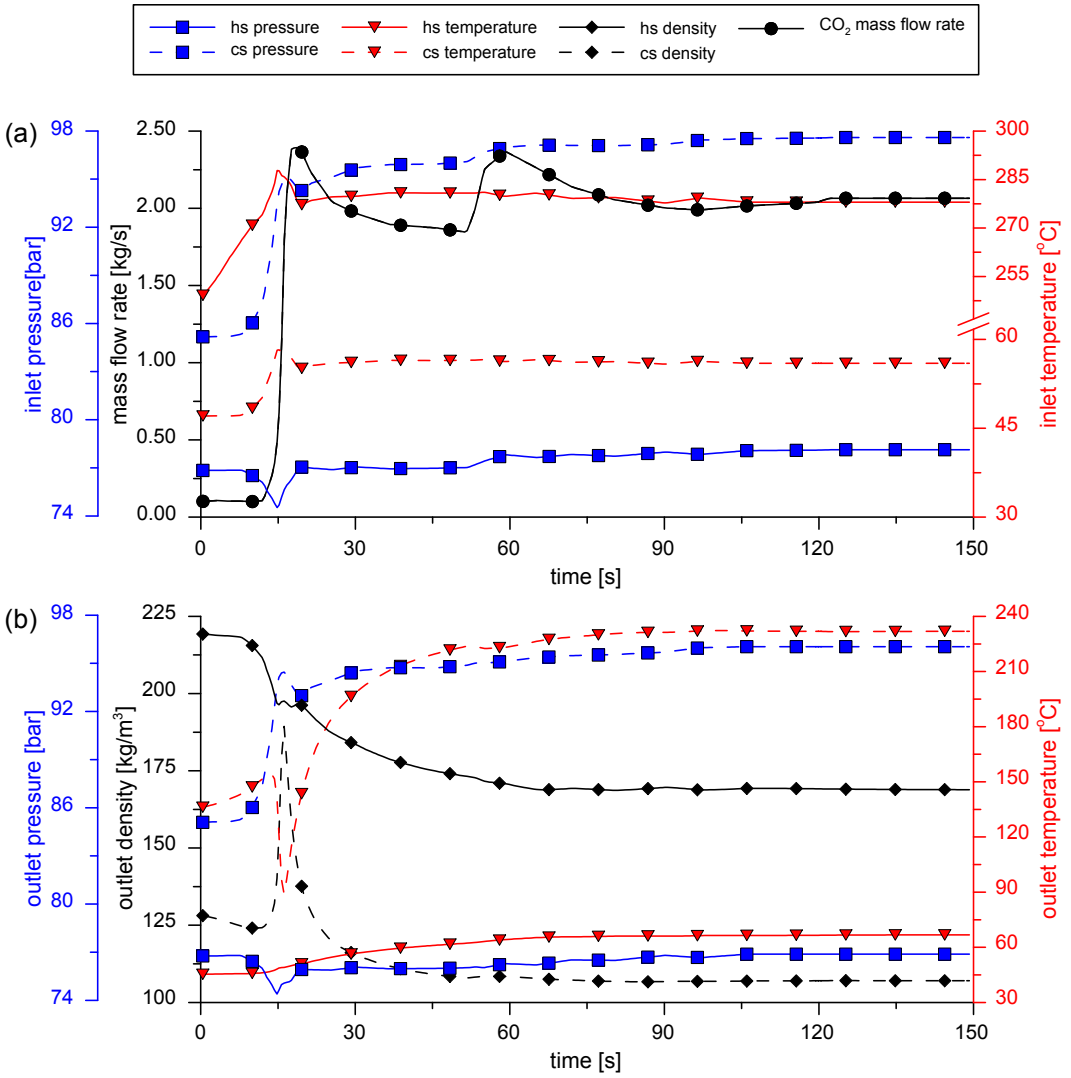


**Fig. 8.** Transient behaviour of the printed circuit recuperator during the start-up of a $sCO_2$ power system: input (a) and output (b) thermodynamic variables.

is worth noting that low initial flow rate allows the $sCO_2$ loop to warm up. This explains why the temperature graphs do not start from ambient conditions. Another important aspect to note is the initial values of the pressure inside the $sCO_2$ loop, which are above the critical point on both sides of the heat exchanger to prevent any liquid formation that would be problematic for the operation of the compressor. Fig. 8b shows how the pressure, temperature and $CO_2$ density vary at the outlet of the PCHE. It can be seen that at start-up there is a substantial drop in the density of the hot and cold $sCO_2$ flow streams at the outlet of the heat exchanger from 247 kg/m$^3$ to 167 kg/m$^3$ and from 150 kg/m$^3$ to 107 kg/m$^3$ respectively. This corresponds to a volumetric expansion of 32.4% and 28.7%. To decrease the magnitude of this expansion which can be risky for the components in the system, the rate at which the mass flow rate or the temperature rise increase should be reduced.

### 4.3.2. Shutdown

The results of the simulations relating to the shutdown of the system are shown in Fig. 9. The input profiles are displayed in Fig. 9.a. After 67 s, the mass flow rate is decreased from an average value of 2.06 kg/s to 0.10 kg/s in approximately 70 s. Unlike the start-up phase, mass flow rate and pressure trends are not synchronised; this could be because of the opening of a bypass valve in the $sCO_2$ loop. After approximately 120 s, the heat source of the $sCO_2$ loop is switched off and, in 15–20 s, the system reaches an idle state. In particular, the temperature at the inlet of the hot side decreases from 279 °C to 248 °C while the hot side inlet pressure remains constant at an average value of 77 bar, which is the lowest of the cycle. On the cold side, the temperature of the cold flow drops from 53 °C to around 47 °C after a small transient, while the pressure decreases from 96 bar to 85 bar. At the heat exchanger outlet, the cold side temperature follows the trend dictated by the hot side inlet. In shutting down the heat source (Fig. 9a), there is a small delay in the temperature response of the PCHE due to its thermal inertia. The pressure also decreases in response to the conditions imposed at the inlet of the PCHE. The outlet density of the cold flow decreases from 112 kg/m$^3$ to 96 kg/m$^3$, which indicates a negligible thermal expansion during the shut-down of the power unit. Inversely, the density at the hot side outlet increases from 162 kg/m$^3$ to 195 kg/m$^3$ due to a slight decrease of the outlet temperature from 105 °C to 88 °C (Fig. 9b).

### 4.3.3. Change of operating conditions

Results related to the change of the system operating conditions are shown in Fig. 10. The mass flow rate of the working fluid circulating in

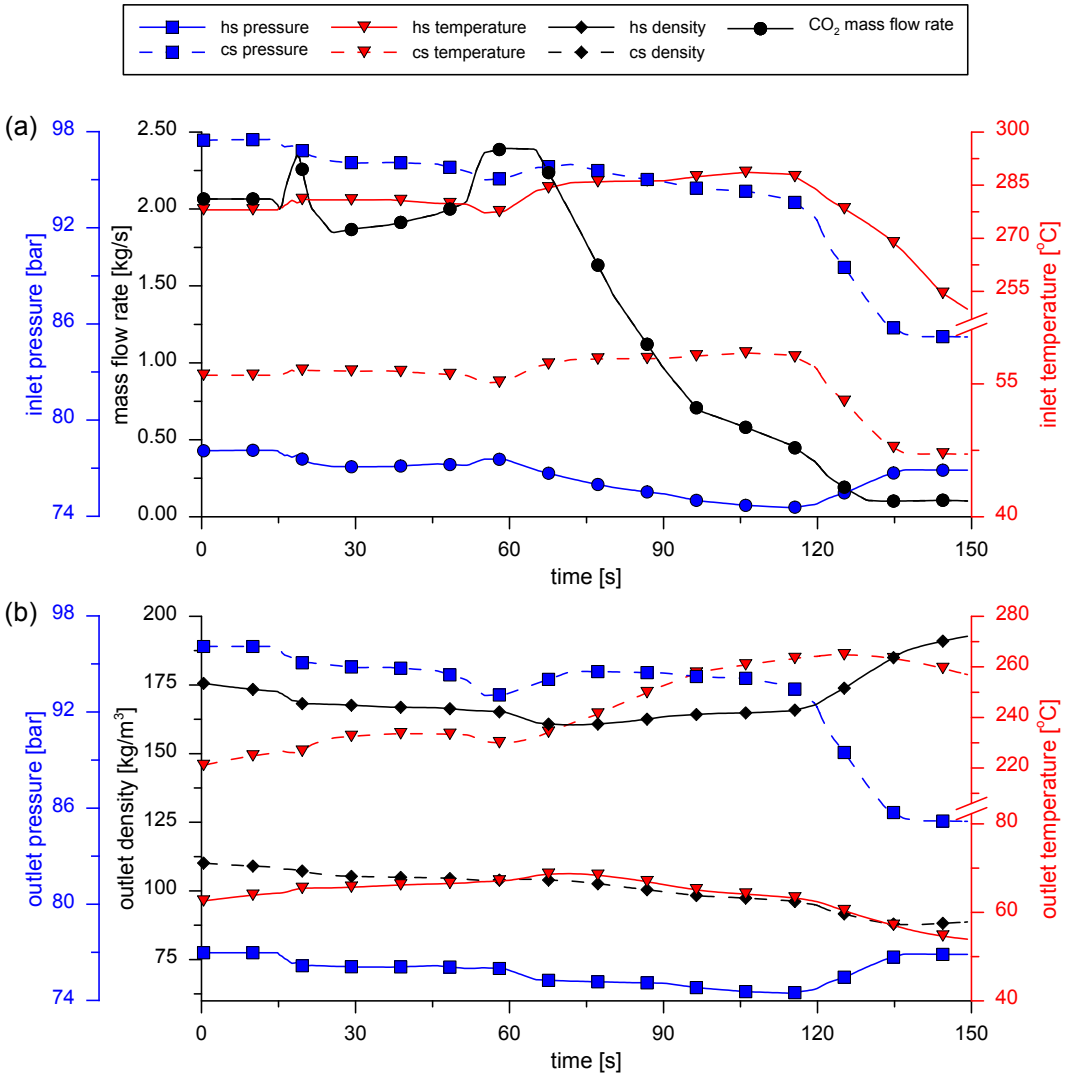


**Fig. 9.** Transient behaviour of the printed circuit recuperator during the shutdown of a $sCO_2$ power system: input (a) and output (b) thermodynamic variables.

the $sCO_2$ power unit is increased from 1.51 kg/s up to 2.10 kg/s (Fig. 10a) by gradually increasing the compressor revolution speed from 37,500 RPM to 52,000 RPM in the period 75–123 s. Since the heat source is operated at the same power level, the temperature of the hot side decreases from 265 °C to 253 °C due to the higher working fluid mass flow rate. The transient behaviour of the pressure profiles at the inlet of the heat exchanger follows the same dynamics of the mass flow rate. In particular, the hot side inlet pressure increases from 100 bar to 104 bar while the cold side rises from 116 bar to 141 bar. The inlet temperature of the cold side also experiences a slight increase from 41 °C to 44 °C (Fig. 10a), due to the higher cycle pressure ratio of the compressor. Analysing the results obtained at the outlet of the PCHE, it is possible to notice that the different operating point does not produce a considerable thermal expansion (Fig. 10b), since the hot side outlet temperature slightly decreases. The pressures change according to the variations occurring at the heat exchanger inlet. The above indicates that using a gradual variation in the speed of the turbomachinery can achieve a smooth variation in all the other operating parameters which reduces sharp increases in the stresses of the components.

## 5. Conclusions

This study assessed the potential and limitations of a 1-D modelling methodology for Printed Circuit Heat Exchangers (PCHEs) used as recuperators in $sCO_2$ power applications. Comparison between the 1-D results with the results of 3-D CFD modelling showed a difference of only 2% confirming the validity of the 1-D modelling methodology for transient simulations. However, the 1-D simulations were not able to predict complex phenomena such as the entry effects in the heat transfer channels.

The 1-D modelling methodology was used to develop performance maps that show the interrelationships and influence of operating conditions on the performance of the PCHE. These characteristics can be used for the selection of design conditions for the system and the impact of off-design operation on system performance.

The transient analysis during start up, shutdown and change of operating point in the $sCO_2$ power system where the PCHE recuperator is installed, confirmed that attention must be paid during the start-up of the $sCO_2$ power unit, to reduce stresses in the system components from sudden changes in the working fluid density and thermal and mechanical shock in the heat exchangers. Slow changes in the speed of the turbomachinery avoid sudden changes in the sCO2 fluid characteristics circulating in the system, reducing the impact from changes in the fluid density. A slow shut-down process with the heat source switched off first whilst the turbomachinery is running can also avoid the negative impacts from the sudden changes in the $sCO_2$ density.

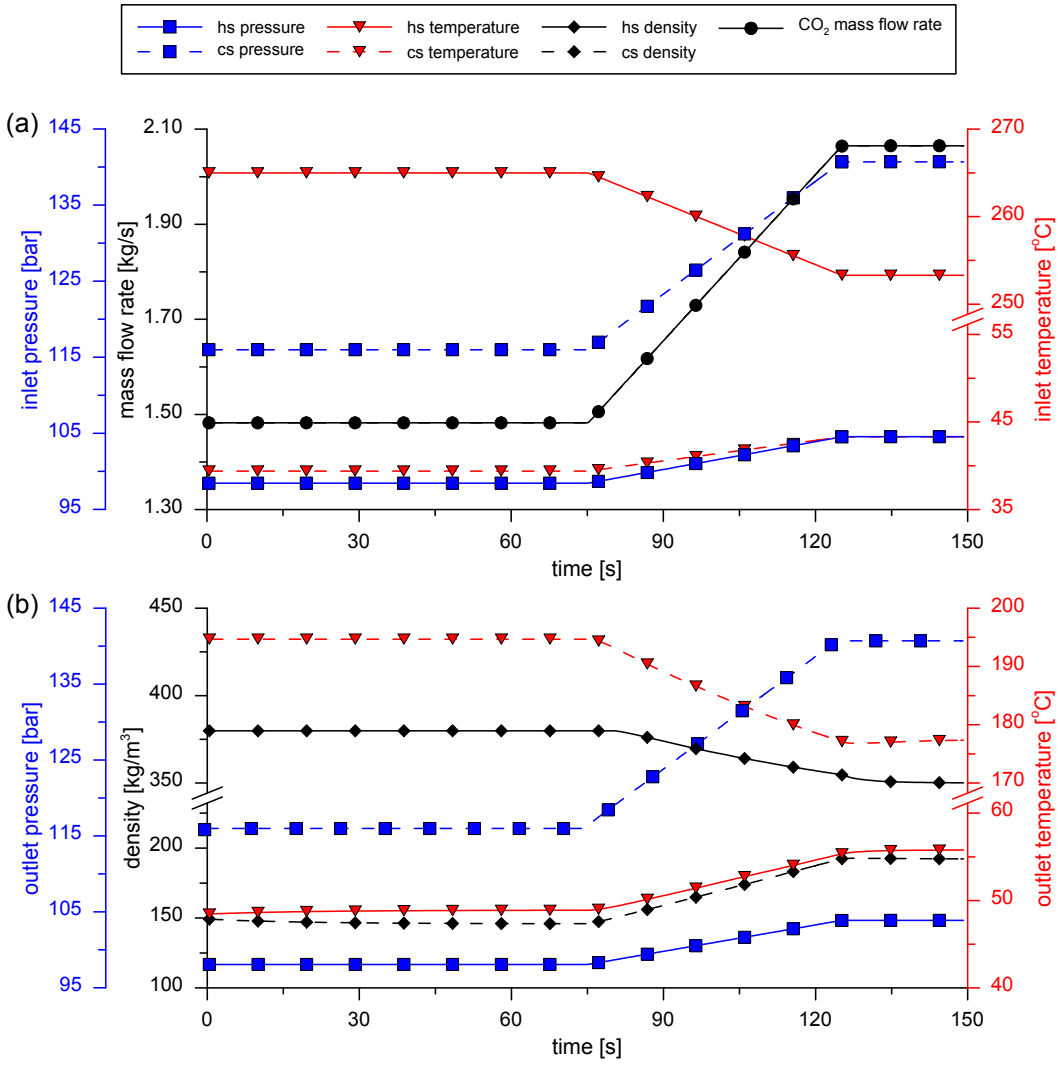


**Fig. 10.** Transient behaviour of the printed circuit recuperator during the change of operating conditions of a $sCO_2$ power system: input (a) and output (b) thermodynamic variables.

## Acknowledgements

The work presented in this paper is supported by a number of funders as follows: (i) The Engineering and Physical Sciences Research Council (EPSRC) of the UK under research grants EP/P004636/1 'Optimising Energy Management in Industry – OPTEMIN', and EP/K011820/1 (Centre for Sustainable Energy Use in Food Chains); (ii) the European Union's Horizon 2020 research and innovation programme under grant agreement No. 680599 for project Industrial Thermal Energy Recovery and Management 'I-ThERM'. The Authors would like to acknowledge the financial support received from the project funders and the industry partners. The manuscript reports all the relevant data to support the understanding of the results. More detailed information and data, if required, can be obtained by contacting the corresponding author of the paper.

## Appendix A. Supplementary material

Supplementary data to this article can be found online at https://doi.org/10.1016/j.applthermaleng.2019.114190.

## References

[1] M. Persichilli, A. Kacludis, E. Zdankiewicz, T. Held, Supercritical $CO_2$ power cycle developments and commercialization: why $sCO_2$ can displace steam steam, Power-Gen India & Central Asia 2012, 2012, pp. 19–21 http://www.echogen.com/documents/why-sCO2-can-displace-steam.pdf.

[2] M. Marchionni, G. Bianchi, S.A. Tassou, Techno-economic assessment of Joule-Brayton cycle architectures for heat to power conversion from high-grade heat sources using $CO_2$ in the supercritical state, Energy 148 (2018) 1140–1152, https://doi.org/10.1016/J.ENERGY.2018.02.005.

[3] K. Brun, P. Friedman, R. Dennis, Fundamentals and applications of supercritical carbon dioxide (sCO2) based power cycles, 2017.

[4] V. Dostal, M. Driscoll, P. Hejzlar, Supercritical $CO_2$ cycle for fast gas-cooled reactors, Expo 2004, (2004) (Accessed March 24, 2017), http://proceedings.asmedigitalcollection.asme.org/proceeding.aspx?articleid=1642908.

[5] G.O. Musgrove, R. Le Pierres, J. Nash, Heat exchangers for supercritical $CO_2$ power cycle applications, The 4th International Symposium for Supercritical $CO_2$ Power Cycles, 2014, pp. 1–61.

[6] Y. Jiang, E. Liese, S.E. Zitney, D. Bhattacharyya, Optimal design of microtube recuperators for an indirect supercritical carbon dioxide recompression closed Brayton cycle, Appl. Energy 216 (2018) 634–648, https://doi.org/10.1016/J.APENERGY.2018.02.082.

[7] A.S. Alsagri, A. Chiasson, A. Aljabr, Thermodynamic analysis and multi-objective optimizations of a combined recompression sCO2 brayton cycle: tCO2 rankine cycles for waste heat recovery, in: Heat Transfer and Thermal Engineering, ASME, vol. 8A, 2018, p. V08AT10A044. doi:10.1115/IMECE2018-86844.

[8] M. Saeed, M.-H. Kim, Analysis of a recompression supercritical carbon dioxide power cycle with an integrated turbine design/optimization algorithm, Energy 165 (2018) 93–111, https://doi.org/10.1016/J.ENERGY.2018.09.058.

[9] M. Atif, F.A. Al-Sulaiman, Energy and exergy analyses of solar tower power plant driven supercritical carbon dioxide recompression cycles for six different locations, Renew. Sust. Energy Rev. 68 (2017) 153–167, https://doi.org/10.1016/J.RSER.2016.09.122.

[10] M.T. Luu, D. Milani, R. McNaughton, A. Abbas, Dynamic modelling and startup

operation of a solar-assisted recompression supercritical $CO_2$ Brayton power cycle, Appl. Energy 199 (2017) 247–263, https://doi.org/10.1016/J.APENERGY.2017.04.073.
[11] S.A. Wright, R.F. Radel, M.E. Vernon, G.E. Rochau, P.S. Pickard, Operation and Analysis of a Supercritical CO2 Brayton Cycle, SANDIA Report SAND2010-0171, 2010, 101.
[12] Q. Li, G. Flamant, X. Yuan, P. Neveu, L. Luo, Compact heat exchangers: a review and future applications for a new generation of high temperature solar receivers, Renew. Sust. Energy Rev. 15 (2011) 4855–4875, https://doi.org/10.1016/J.RSER.2011.07.066.
[13] K. Nikitin, Y. Kato, L. Ngo, Printed circuit heat exchanger thermal–hydraulic performance in supercritical $CO_2$ experimental loop, Int. J. Refrig. 29 (2006) 807–814, https://doi.org/10.1016/J.IJREFRIG.2005.11.005.
[14] T.L. Ngo, Y. Kato, K. Nikitin, T. Ishizuka, Heat transfer and pressure drop correlations of microchannel heat exchangers with S-shaped and zigzag fins for carbon dioxide cycles, Exp. Therm. Fluid Sci. 32 (2007) 560–570, https://doi.org/10.1016/J.EXPTHERMFLUSCI.2007.06.006.
[15] S.-M. Lee, K.-Y. Kim, A parametric study on fluid flow and heat transfer in a printed circuit heat exchanger, in: ASME/JSME 2011 8th Thermal Engineering Joint Conference, ASME, 2011, pp. T10063–T10063-6. doi:10.1115/AJTEC2011-44629.
[16] S.-M. Lee, K.-Y. Kim, Optimization of zigzag flow channels of a printed circuit heat exchanger for nuclear power plant application, J. Nucl. Sci. Technol. 49 (2012) 343–351, https://doi.org/10.1080/00223131.2012.660012.
[17] S.-M. Lee, K.-Y. Kim, Comparative study on performance of a zigzag printed circuit heat exchanger with various channel shapes and configurations, Heat Mass Transfer 49 (2013) 1021–1028, https://doi.org/10.1007/s00231-013-1149-4.
[18] S.-M. Lee, K.-Y. Kim, A parametric study of the thermal-hydraulic performance of a zigzag printed circuit heat exchanger, Heat Transfer Eng. 35 (2014) 1192–1200, https://doi.org/10.1080/01457632.2013.870004.
[19] S.-M. Lee, K.-Y. Kim, Multi-objective optimization of arc-shaped ribs in the channels of a printed circuit heat exchanger, Int. J. Therm. Sci. 94 (2015) 1–8, https://doi.org/10.1016/J.IJTHERMALSCI.2015.02.006.
[20] S.G. Kim, Y. Lee, Y. Ahn, J.I. Lee, CFD aided approach to design printed circuit heat exchangers for supercritical $CO_2$ Brayton cycle application, Ann. Nucl. Energy 92 (2016) 175–185, https://doi.org/10.1016/J.ANUCENE.2016.01.019.
[21] Y.-J. Baik, S. Jeon, B. Kim, D. Jeon, C. Byon, Heat transfer performance of wavy-channeled PCHEs and the effects of waviness factors, Int. J. Heat Mass Transfer 114 (2017) 809–815, https://doi.org/10.1016/J.IJHEATMASSTRANSFER.2017.06.119.
[22] S.Y. Lee, B.G. Park, J.T. Chung, Numerical studies on thermal hydraulic performance of zigzag-type printed circuit heat exchanger with inserted straight channels, Appl. Therm. Eng. 123 (2017) 1434–1443, https://doi.org/10.1016/J.APPLTHERMALENG.2017.05.198.
[23] Q. Chen, Entransy dissipation-based thermal resistance method for heat exchanger performance design and optimization, Int. J. Heat Mass Transfer 60 (2013) 156–162, https://doi.org/10.1016/J.IJHEATMASSTRANSFER.2012.12.062.
[24] Q. Chen, J.-H. Hao, T. Zhao, An alternative energy flow model for analysis and optimization of heat transfer systems, Int. J. Heat Mass Transfer 108 (2017) 712–720, https://doi.org/10.1016/J.IJHEATMASSTRANSFER.2016.12.080.
[25] S.-Y. Zhao, Q. Chen, A thermal circuit method for analysis and optimization of heat exchangers with consideration of fluid property variation, Int. J. Heat Mass Transfer 99 (2016) 209–218, https://doi.org/10.1016/J.IJHEATMASSTRANSFER.2016.03.124.
[26] G. Bianchi, S.S. Saravi, R. Loeb, K.M. Tsamos, M. Marchionni, A. Leroux, Design of a high-temperature heat to power conversion facility for testing supercritical $CO_2$ equipment and packaged power units, Energy Proc. 161 (2019) 421–428, https://doi.org/10.1016/J.EGYPRO.2019.02.109.
[27] L. Chai, S.A. Tassou, Numerical study of the thermohydraulic performance of printed circuit heat exchangers for supercritical $CO_2$ Brayton cycle applications, Energy Proc. 161 (2019) 480–488, https://doi.org/10.1016/j.egypro.2019.02.066.
[28] E.W. Lemmon, M.L. Huber, M.O. Mclinden, NIST Reference Fluid Thermodynamic and Transport Properties— REFPROP User's Guide, 2013.
[29] T.K. Serghides, Estimate friction factor accurately, Chemical Engineering (New York), vol. 91, 1984, pp. 63–64.
[30] V. Gnielinski, New equation for heat and mass transfer in turbulent pipe and channel flow, Int. Chem. Eng. 16 (1976) 359–368.
[31] Gamma Technologies Inc, GT-SUITE-Flow Theory Manual, 2019.
[32] L. Chai, S.A. Tassou, Effect of cross-section geometry on the thermohydraulic characteristics of supercritical $CO_2$ in minichannels, Energy Proc. 161 (2019) 446–453, https://doi.org/10.1016/J.EGYPRO.2019.02.077.
[33] L. Cheng, G. Ribatski, J.R. Thome, Analysis of supercritical $CO_2$ cooling in macro- and micro-channels, Int. J. Refrig. 31 (2008) 1301–1316, https://doi.org/10.1016/J.IJREFRIG.2008.01.010.
[34] M. Anderson, R. Fatima, M. Corradini, A. Towne, D. Ranjan, Alan Kruizenga Heat Transfer of Supercritical Carbon Dioxide in Printed Circuit Heat Exchanger Geometries, 2011. doi:10.1115/1.4004252.
[35] M. De Miol, G. Bianchi, G. Henry, N. Holaind, S.A. Tassou, A. Leroux, Design of a single-shaft compressor, generator, turbine for small-scale supercritical $CO_2$ systems for waste heat to power conversion applications, 2nd European $sCO_2$ Conference 2018, 2018, https://doi.org/10.17185/DUEPUBLICO/46086.
[36] E.M. Clementoni, T.L. Cox, C.P. Sprague, Startup and operation of a supercritical carbon dioxide brayton cycle, V008T34A006, J. Eng. Gas Turb Power 136 (2014), https://doi.org/10.1115/GT2013-94275.